ISOCAM observations of the Ursa Major cirrus:

Evidence for large abundance variations of small dust grains

M.-A. Miville-Deschênes[1,2,3]**, F. Boulanger**[1]**, G. Joncas**[2] **and E. Falgarone**[3]

[1] Institut d'Astrophysique Spatiale, Université Paris-Sud, Bât. 121, 91405, Orsay, France
[2] Département de Physique, Université Laval, Sainte-Foy, Québec, G1K 7P4, Canada
[3] Laboratoire de radioastronomie, École Normale Supérieure, 24 rue Lhomond, 75005, Paris, France

Abstract. We present mid-IR imaging observations of a high Galactic latitude cirrus obtained with the ISO camera ISOCAM at 6" angular resolution. The observations were done with two filters LW2 (5-8.5 μm) and LW3 (12-18 μm) that measure respectively the aromatic carbon bands and the underlying continuum emission from small dust particles. Three 0.05 square degree images sample atomic and molecular sections in the Ursa Major cirrus. These images are compared with H I , CO and IRAS observations. In such a cloud transparent to stellar light ($A_V < 0.5$) the mid-infrared to 100 μm and the mid-IR emissivity per hydrogen are related to the abundance and the optical properties of small dust particles independently of any modelling of the penetration of the radiation. Within the atomic section of the cloud, the comparison between ISOCAM images and 21 cm interferometric data highlights an enhancement of the mid-IR emitters abundance by a factor ~ 5 in an H I filament characterized by a large transverse velocity gradient suggestive of rotation. Furthermore, a drop in the abundance of the same mid-IR emitters is observed at the interface between the atomic and molecular cirrus sections. We propose that these abundance variations of the mid-IR emitters are related to the production of small dust particles by grain shattering in energetic grain-grain collisions generated by turbulent motions within the cirrus and inversely by their disappearance due to coagulation on large grains. At the H I-H$_2$ interface we also observe a change in the $I_\nu(\text{LW2})/I_\nu(\text{LW3})$ ratio by a factor 2. This color variation indicates that the amplitude of the continuum near 15 μm, relative to the aromatic bands, rises inside the molecular region. It could result from a modification of the dust size distribution or of the intrinsic optical properties of the small dust particles.

Key words. interstellar medium; infrared cirrus; dust; turbulence.

1. Introduction

We know that interstellar dust plays an important role in the physics of the interstellar medium. For instance, dust grains heat the gas via the photoelectric effect (Bakes & Tielens, 1994) and provide the surfaces necessary to the formation of H$_2$ (Duley & Williams, 1993). These processes are sensitive to the size distribution, the structure and composition of dust grains and, especially, to the abundance of the smallest particles. The IRAS images of nearby molecular complexes and bright cirrus clouds ($A_V > 1$) have been extensively used to compare the spatial distribution of the mid-IR emission from the smallest stochastically heated grains and that of the far-IR emission from larger grains in thermal equilibrium. The color ratio between these two emissions has been related to the abundance ratio between small and large dust grains

which was inferred to widely vary from cloud to cloud and within clouds (Boulanger et al., 1990). The gain in brightness sensitivity and angular resolution provided since then by dedicated observations carried out with ISOCAM, the camera on board the Infrared Space Observatory (ISO), now allows us to carry on these IRAS investigations and in particular to extend them to the range of column densities ($N_H \sim 5 \times 10^{20}$ cm^{-2}) where the transition from atomic to molecular gas takes place.

ISOCAM has provided low resolution spectra ($\lambda/\Delta\lambda \sim 50$) of the mid-IR interstellar emission over a wide range of environments including the diffuse Galactic emission and cirrus clouds. The emission in the 3-15 μm range is invariably associated with emission bands considered to be characteristic of aromatic hydrocarbon particles. To be heated to temperatures of a few 100 K by single stellar photons these particles have to be smaller than a few thousands carbon atoms. The exact nature, structure and origin of the emitting particles are still a matter of debate.
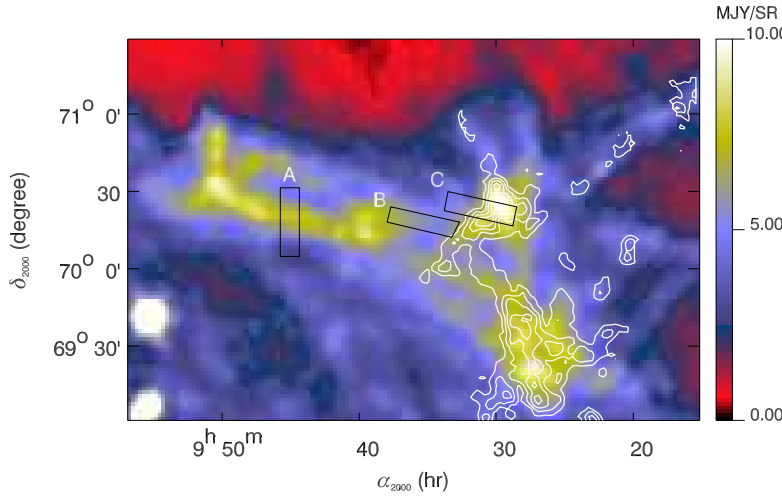
Fig. 1. The Ursa Major cirrus observed by IRAS at 100 μm (color map) with the CO integrated emission of Pound & Goodman (1997) in contours (first level = 5 K km s^{-1} and step is also 5 K km s^{-1}). The position of the three ISOCAM fields observed are also shown.

The abundance variations revealed by IRAS images show that small dust grains might not be related to the particles released by evolved stars and could be formed within the interstellar medium (Henning, 1999). It is the motivation of this work to shed further light on the evolution of small dust grains within the diffuse interstellar medium in relation to gas physical conditions. To do this we have combined ISOCAM observations of the Ursa Major cirrus cloud with 21 cm, CO and IRAS data. The Ursa Major cirrus has a moderate opacity to stellar light (A$_V$ < 0.5) and an atomic and molecular sections traced by H$_I$ and CO emission respectively. The comparison of these data sets allows us to measure the mid-IR emissivity per hydrogen which, in a cloud transparent to stellar light, is related to the abundance and the optical properties of small dust particles independently of any modelling of the penetration of the dust heating radiation.

The observations used in this investigation are presented in § 2. The structure and the kinematics of the Ursa Major cirrus is described in § 3. In § 4 we estimate the emissivity per H atom of small dust grains in the atomic part. Section 5 is devoted to the estimate of the abundance of small dust grains in an H$_I$ filament with a particular kinematic and § 6 addresses the same question for the H$_I$-H$_2$ interface. The relation between the spatial variations of the dust emission and the gas physical conditions are discussed in § 7. The main results of this analysis are summarized in § 8.

2. Observations and data processing

We present ISOCAM observations of the Ursa Major cirrus, a piece of the North Celestial Loop (Heiles, 1989) (see Fig. 1). This cirrus is composed of two connected parts, one predominantly atomic, detected only in the H$_I$ line
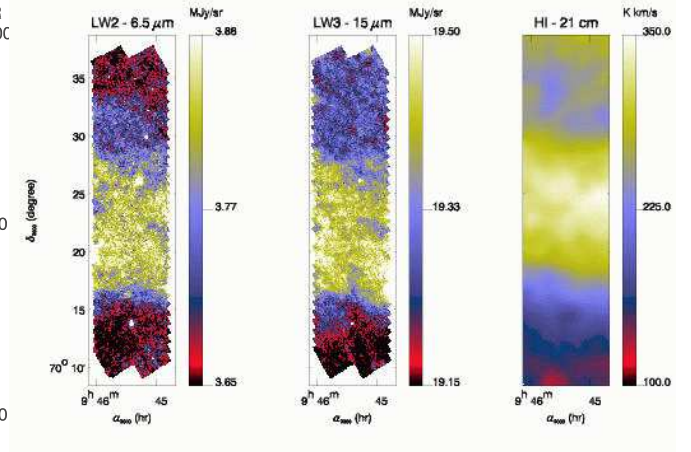
Fig. 2. Field A : LW2 image (**left**), LW3 image (**middle**) and 21 cm integrated emission map (**right**).

and one mostly molecular, detected in CO (de Vries et al., 1987; Pound & Goodman, 1997). For the sake of simplicity we will name these two sections of the cirrus *atomic* and *molecular* in the following. The atomic section of the cirrus is representative of the so called H$_I$ clouds with a density $n \sim 100$ cm^{-3} and a temperature $T \sim 200$ K (Joncas et al., 1992). It is illuminated by the mean solar neighbourhood interstellar radiation field (ISRF) and it is optically thin to this radiation; the H$_I$ column densities range from 2 to 6×10^{20} cm^{-2}. According to de Vries et al. (1987), the distance of the Ursa Major cirrus is $\sim$100 pc.
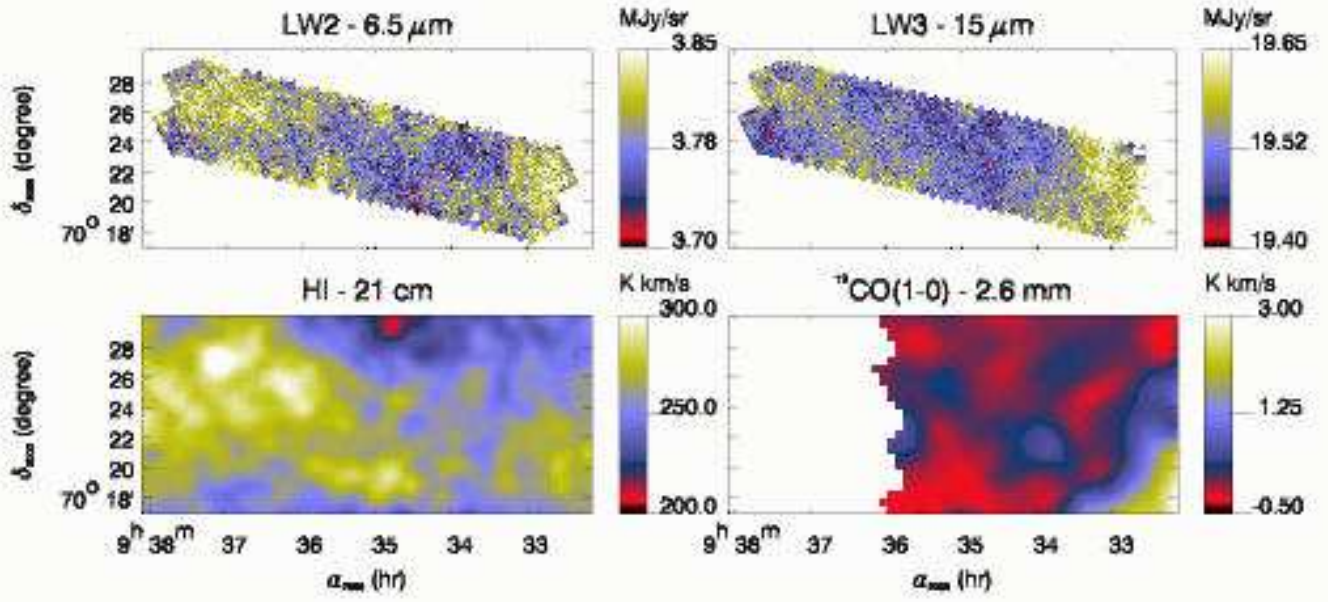
2.1. ISOCAM observations

Three small fields of 0.05 square degree have been mapped with ISOCAM (see Table 1 for the observation log). The location of the three fields is indicated in Fig. 1. These fields have been selected according to the following criteria. First, field A crosses an H$_I$ filament with a large transverse velocity gradient suggesting a rotation along the long axis (Miville-Deschênes, 1999). It provides the opportunity of studying the impact of this peculiar gas velocity distribution upon the spatial and size distributions of small dust particles. Secondly, fields B and C encompass an atomic-molecular interface, allowing the analysis of dust properties variations across this interface.

The ISOCAM observations were made in the LW2 (5 to 8.5 μm) and LW3 (12 to 18 μm) broad band filters. For diffuse clouds the emission in these filters is dominated by the zodiacal emission; the contrast of the cirrus is as small as a few 0.1 per cent in the LW3 filter. Furthermore, ISOCAM is affected by instrumental effects that can be one order of magnitude higher than the contrast we are looking for. To correct for these instrumental effects we have developed a data processing method based on the fact that a given point on the sky has been observed several times. This method is described in Miville-Deschênes et al. (2000). Without this particular data processing, the ISOCAM observations presented in this paper would have

|	field A	field B	field C
Filters	LW2 and LW3	LW2 and LW3	LW2 and LW3
Right Ascension (J2000)	9h 45m 24.8s	9h 35m 7.4s	9h 30m 45.6s
Declination (J2000)	70° 22' 54.8"	70° 23' 15.1"	70° 26' 48.4"
Total number of readouts	490	487	490
Number of sky positions	2×32	2×32	2×32
Number of readouts per sky position	5	5	5
Step size between subsequent positions (pixels)	8	8	8
Integration time (seconds)	5.04	5.04	5.04
Lens (pixel field of view)	6"	6"	6"

Table 1. Description of the ISOCAM observations. The LW2 and LW3 broad filters correspond respectively to the wavelength ranges [5-8.5] and [12-18] μm. The size of the three fields is $\sim 7' \times 26'$.

Fig. 3. ISOCAM (LW2 and LW3), HI and CO observations of field B.
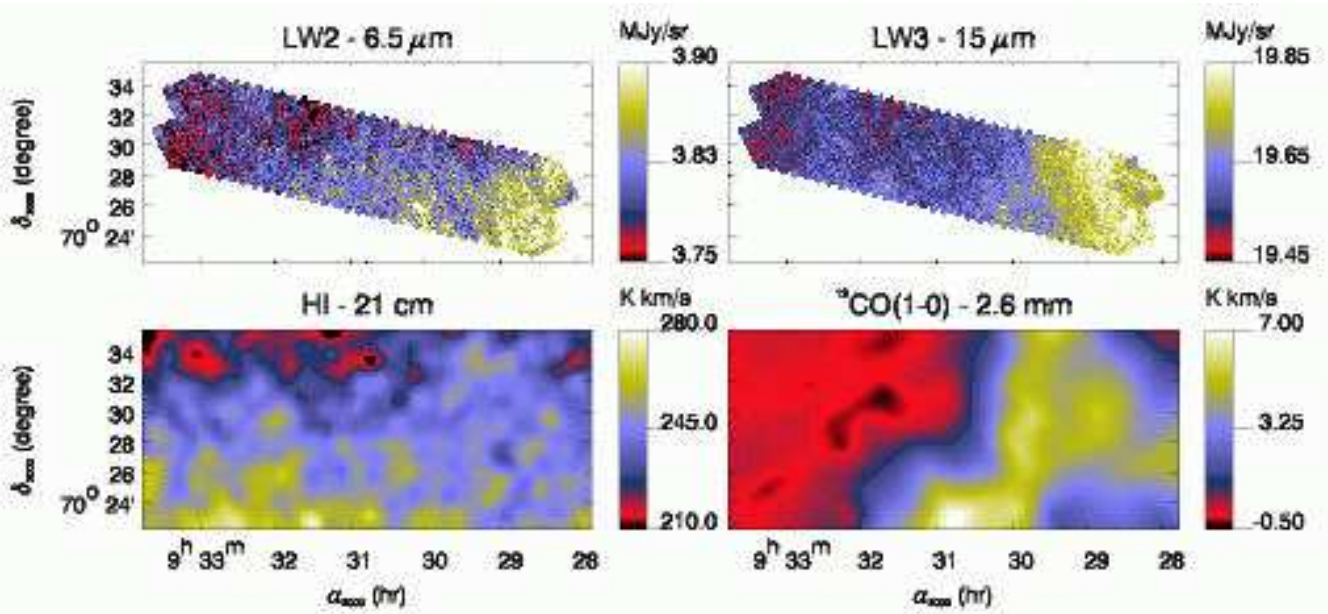
Fig. 4. ISOCAM (LW2 and LW3), HI and CO observations of field C.
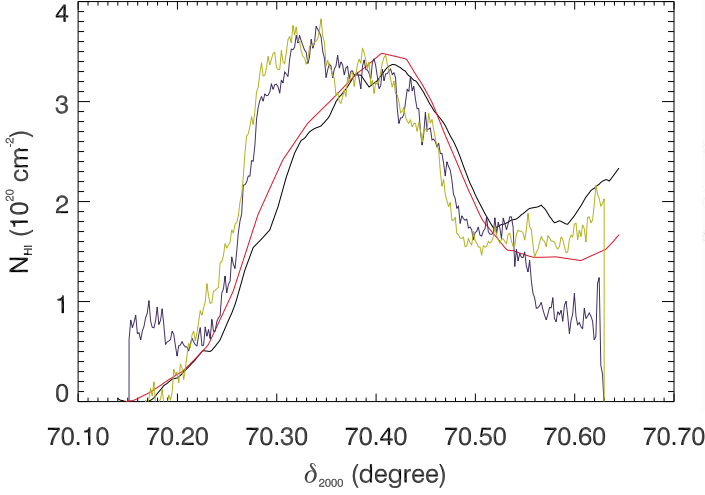
Fig. 5. Column density profiles as a function of the declination in field A for the H I column density (black), LW2 (blue), LW3 (yellow) and IRAS 100 μm (red). An offset has been subtracted to each profile (taken at the southern edge of the field). All the infrared emission profiles were normalized to the H I column density by constant factors: $N_{\mathrm{LW2}} = (I_{\mathrm{LW2}} - 3.61)/6.5 \times 10^{-22}$, $N_{\mathrm{LW3}} = (I_{\mathrm{LW3}} - 19.12)/9.0 \times 10^{-22}$ and $N_{100} = (I_{100} - 2.7)/1.4 \times 10^{-20}$

been useless. The LW2 and LW3 images of the three fields are shown in Figures 2, 3 and 4. The mid-infrared peak-to-peak fluctuations in these images are $\lesssim 0.4$ MJy sr^{-1} and the rms of the high frequency noise is ~ 0.02 MJy sr^{-1}.

2.2. H I *and CO observations*

We have combined the mid-infrared observations with CO and H I observations to conduct our analysis. The H I (21 cm) observations were obtained at the Dominion Radio Astrophysical Observatory of Penticton (Canada). Part of these data were published by Joncas et al. (1992) and the whole set will be the subject of a forthcoming paper (Miville-Deschênes, 1999; Miville-Deschênes et al., 2001). The spatial resolution of these 21 cm observations is 1' and the spectral resolution is 0.66 km s^{-1}.

In order to compare the dust emission with the whole gas content, we use ^{12}CO observations of the Ursa Major cirrus in the J=(1-0) transition at 115.271203 GHz that were obtained by Pound & Goodman (1997). These authors kindly let us use their data obtained with a Gaussian beam of 100" and a velocity resolution of 0.27 km s^{-1}. The images of the integrated H I and CO emission of the three ISOCAM fields are also shown in Figures 2, 3 and 4.

3. General structure and kinematics

3.1. Field A - an H I *filament*
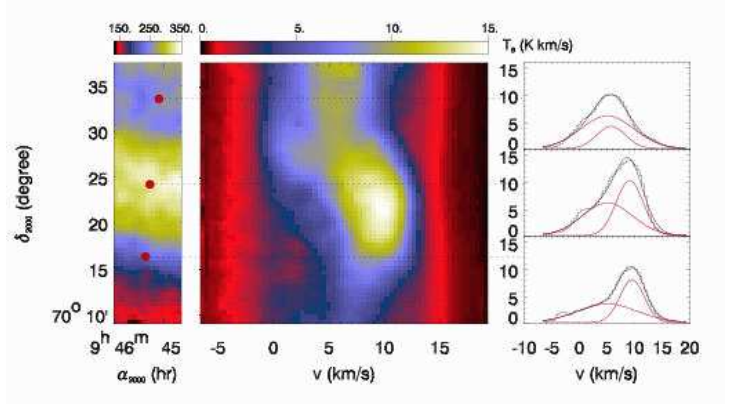
Fig. 6. Left: map of the 21 cm integrated flux in field A. Center: position (δ_{2000})-velocity representation of the 21 cm data. Right: three typical spectra with the result of the Gaussian decomposition. The positions of the three spectra are indicated with red points and dotted lines.

3.1.1. Comparison of dust and gas tracers

The field A observed by ISOCAM is a small cut across a filament (length ~ 5 pc and width ~ 0.5 pc), observed in all IRAS bands (see the 100 μm emission in Fig. 1) and at 21 cm (Joncas et al., 1992). As seen in Fig. 2, the filament is also well detected in the mid-infrared. The CO observations of Pound & Goodman (1997) do not include field A, but CO has been searched unsuccessfully at the 0.1 K level within this area by de Vries et al. (1987) and G. Lagache (private communication). Therefore we will consider that field as predominantly atomic and use the 21 cm data as a tracer of the spatial structure and kinematic of the gas.

On a large scale, the structure in the LW2 and LW3 broad band filters is very similar to the H I emission. But a careful comparison of the spatial distribution of the mid-infrared and H I emissions reveals significant discrepancies. In Fig. 5 we plot the total H I column density, the LW2, LW3 and IRAS 100 μm brightness, averaged over α_{2000}, as a function of the declination δ_{2000} in field A. In these profiles, the emission in the LW2 and LW3 filters and the 100 μm emission have been normalized to the H I column density with a constant ratio. These profiles show that the H I emission is very well correlated to the 100 μm emission, but the peak of the emission in the two ISOCAM filters does not coincide with that of the FIR and H I; the mid-IR emission is shifted compared to the H I and 100 μm emissions.

3.1.2. Kinematics of the gas

The velocity structure of the H I emission within field A is described in Fig. 6. The central panel presents a velocity-position diagram of the 21 cm emission. Three representative H I spectra of this field are also shown in the right panel. On most of the field, the 21 cm spectra are charac-
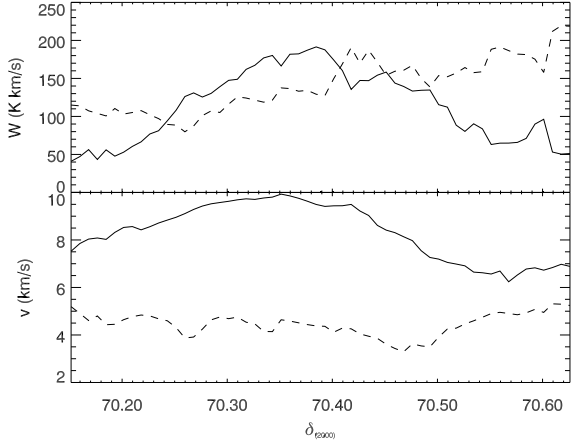
Fig. 7. Upper panel: Mean integrated 21 cm emission as a function of the declination for the two H I components identified by the Gaussian decomposition. Lower panel: mean velocity as a function of the declination for the two components. The continuous line depicts the filament and the dotted line depicts the more diffuse component.

terized by two components. The two components clearly overlap in velocity and it is impossible to separate them only by selecting velocity ranges. To estimate the column density of each component across the field, we decompose the spectra by a sum of two Gaussians. From this decomposition, we derive the integrated intensity, the velocity centroid and the velocity dispersion of each component on the line of sight. The two components correspond to spatially coherent structures which extend beyond the ISOCAM field (Miville-Deschênes et al., 2001). The brightest structure seen in the position-velocity diagram (Fig. 6) at a velocity of ~ 8 km s^{-1} corresponds to the filament observed in the IRAS 100 μm map (Fig. 1). The second component at a central velocity of ~ 4 km s^{-1} is more diffuse; it is also observed beyond field A.

In Fig. 7 we show the mean integrated intensity and the velocity centroid of these two components across field A. The component associated with the filament (solid line in Fig. 7) contributes $\sim 40\%$ of the total integrated emission of the field. It is characterized by two velocity gradients perpendicular to the filament; first there is a 2 km s^{-1} increase of the velocity from $\delta_{2000} = 70.15°$ to $70.35°$ and then a decrease of 4 km s^{-1} from $\delta_{2000} = 70.35°$ to $70.54°$. At a distance of 100 pc, these variations correspond respectively to gradients of $\sim$5 and -10 km s^{-1} pc^{-1}. The velocity dispersion of this component measured on individual spectra is $\sim 2-3$ km s^{-1}. The more diffuse component (dashed line in Fig. 7), which contributes $\sim 60\%$ of the gas emission, is characterized by a north-south integrated emission gradient and an almost constant velocity centroid (~ 4 km s^{-1}). Its velocity dispersion is significantly larger than that of the filament, with values between ~ 6 and 10 km s^{-1}.
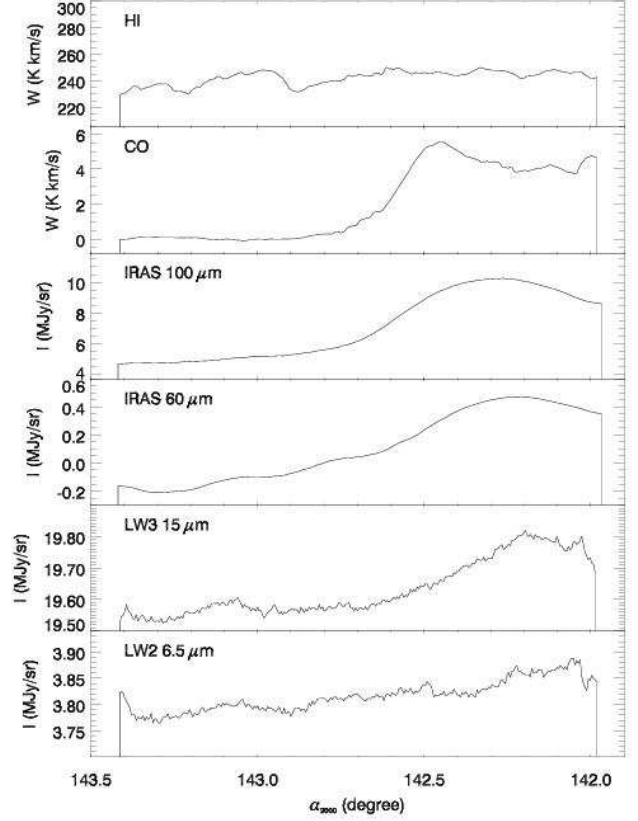

Fig. 8. Mean intensity in field C as a function of α_{2000}. From top to bottom: H I(1'), CO (1.7'), IRAS 100 μm(4'), IRAS 60 μm(3'), LW3 (6") and LW2 (6"). The numbers in parenthesis are the resolutions of the observations.

3.2. Field B and C - an H I -H_2 interface

The two other fields observed with ISOCAM cross an atomic/molecular gas interface as indicated by CO observations. In field B (Fig. 3) there is a slight increase of the CO emission (up to $T_B \sim 3$ K km s^{-1}) at the western edge of the field. The H I emission in this field is very uniform; the contrast in the 21 cm line integrated emission is $\sim$10%.

In field C, H I and CO observations are available for the whole region observed by ISOCAM. There is a slight north-south H I emission gradient but again the contrast is very low ($< 10\%$). Most of the column density variations in field C is associated with CO emission.

In Fig. 8 we show cuts across field C in H I, CO, IRAS 100 μm, IRAS 60 μm, LW2 and LW3. What is striking at first is the flatness of the H I emission. There is a sharp rise of the CO emission near $\alpha_{2000} = 142.6°$, not associated with any change in the H I emission. In contrast, the dust emission in all 4 bands increases in the molecular region, but with less sharpness unrelated to the angular resolution. The infrared dust emission systematically peaks on the western side of the CO filament. Furthermore, we also notice that the peak position of the dust emission at
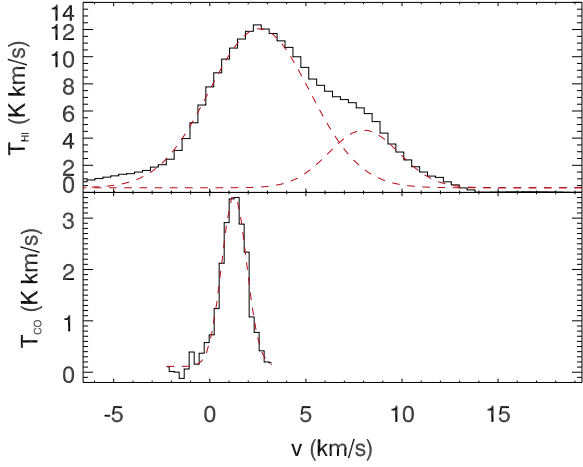
Fig. 9. **Top:** 21 cm spectrum at the position of t̶
CO J=(1-0) peak intensity in field C ($\alpha_{2000} = 9h31m$,
$\delta_{2000} = 70°23'$). **Bottom:** CO spectrum at the same posi-
tion. The result of a Gaussian decomposition of the spec-
tra is also shown (dash lines). Two H$_I$ components are
identified (FWHM of 6.16 and 4.28 km s^{-1}). Only the
largest of the two H$_I$ components is seen in CO (FWHM
of 1.50 km s^{-1}).

Fig. 10. LW2 (**top**) and LW3 (**bottom**) brightness as a
function of the H$_I$ column density (defined in the optically
thin approximation). The linear regression over-plotted
are: I_{LW2} (MJy/sr) $= 6.07 \times 10^{-22} N_{\text{HI}}$ (cm^{-2}) $+ 3.47$ and
I_{LW3} (MJy/sr) $= 8.41 \times 10^{-22} N_{\text{HI}}$ (cm^{-2}) $+ 18.92$

shorter wavelength seems to be more shifted with respect
to the CO emission than at longer wavelength.

In velocity space, the H$_I$ and CO data are very simple
to describe. CO and 21 cm spectra taken at the peak CO
intensity in field C are shown in Fig. 9. These spectra are
representative of both fields B and C. The CO emission is
characterized by a single symmetric component centered
at ~ 1.3 km s^{-1} with a velocity width at half power of
~ 0.7 km s^{-1}. The H$_I$ emission is much broader; the spec-
trum is clearly not symmetric with its peak intensity near
~ 2 km s^{-1}. It can be fitted by two Gaussian components,
one at $v \sim 2.7$ km s^{-1} with a width of ~ 2.7 km s^{-1} and
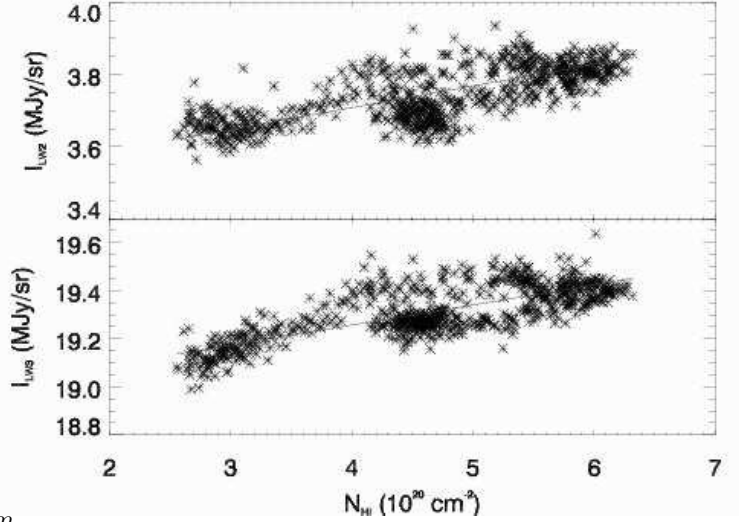a second one at $v \sim 8.5$ km s^{-1} with a width of ~ 2.0 km
s^{-1}.

4. Emissivity of the small dust particles

4.1. Correlation between the mid-infrared emission and the H$_I$ integrated emission

A main goal of this work is to study the relation between
the dust and gas emission. If the dust-to-gas ratio and the
heating of the dust are uniform and constant, the mid-
infrared emission $I_{mir}(\alpha, \delta)$ may be described by:

$$I_{mir}(\alpha, \delta) = e \times N_H(\alpha, \delta) + I_{back} \qquad (1)$$

where e is the dust emissivity, N_H the total column den-
sity of hydrogen (H$_I$ and H$_2$) and I_{back} is the background
level (assumed constant over the observed field). The total
hydrogen column density is deduced from the integrated
emission at 21 cm (W_{HI}): $N_{\text{HI}} = 1.823 \times 10^{18} W_{\text{HI}}$ (Spitzer,
1978) when the atomic gas is optically thin, which we con-
sider a reasonable assumption for this cloud. We did not

look for a correlation between N_H and I_{mir} in fields B
and C because of the very low contrast of the mid-infrared
emission and because of the great uncertainty concerning
the CO to H$_2$ conversion factor (de Vries et al. (1987) give
$N_{H2} = 0.5 \pm 0.3 \times 10^{20} W_{CO}$ cm^{-2} K^{-1} (km/s)$^{-1}$ for the
Ursa Major cirrus).

The LW2 vs N_{HI} and LW3 vs N_{HI} plots in field A are
shown in Fig. 10. The mid-infrared emissions rise globally
with the H$_I$ column density; these relations are approxi-
mately linear (see Fig. 10). Nevertheless, the rms scatter
in the LW2-N_{HI} and LW3-N_{HI} relations (0.05 MJy/sr for
LW2 and 0.07 MJy/sr for LW3) is significantly larger than
the noise level (0.02 MJy/sr).

### 4.2. Background emission in the ISOCAM images

The scatter around the LW2 vs N_{HI} and LW3 vs N_{HI} re-
lations indicates that our description of the mid-infrared
emission with Eq. 1 is probably too simple. This scatter
may originate from a spatial variation of the emissivity or
of the background emission. Here the background level is
mainly due to the zodiacal light, which is uniform at the
scale of our small fields. Therefore we conclude that the
scatter of the LW2 vs N_{HI} and LW3 vs N_{HI} relations in
field A is due to spatial variations of the emissivity e.

In order to quantify the mid-infrared emissivity for
each position (α, δ), the uniform background emission
level of the ISOCAM images must be estimated. This is
also essential to compare the emission between the LW2
and LW3 filters. We can estimate the background level
by inspecting the relation between the mid-infrared fluxes
and the total column density of hydrogen (see Fig 10). If
the mid-infrared flux is, at first order, proportional to the
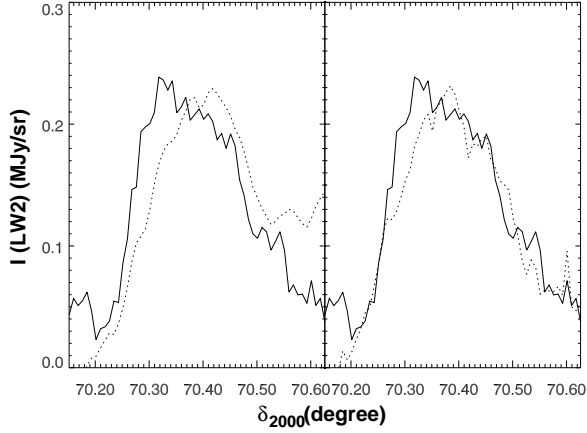
Fig. 11. Mean LW2 flux (at the resolution of the H I observation) as a function of the declination (continuous line). Left: the dotted line is the mid-infrared profile reproduced from the H I data with an emissivity of $e_\nu = 4.5 \times 10^{-22}$ MJy/sr cm^2 (which corresponds to $4\pi\nu e_\nu = 3.8 \times 10^{-31}$ W/H) Right: the dotted line is a reconstruction of the mid-infrared profile with an emissivity of 8.2×10^{-22} MJy/sr cm^2 (4.6×10^{-31} W/H) for the filament and of 1.6×10^{-22} MJy/sr cm^2 (0.9×10^{-31} W/H) for the diffuse component.
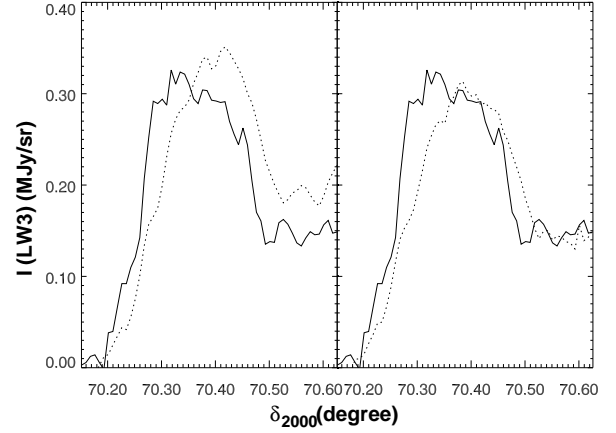
Fig. 12. Mean LW3 flux (at the resolution of the H I observation) as a function of the declination (continuous line). Left: the dotted line is the mid-infrared profile reproduced from the H I data with an emissivity of 7.1×10^{-22} MJy/sr cm^2 (2.3×10^{-31} W/H). Right: the dotted line is a reconstruction of the mid-infrared profile with an emissivity of 1.1×10^{-21} MJy/sr cm^2 (2.5×10^{-31} W/H) for the filament and of 3.8×10^{-22} MJy/sr cm^2 (1.0×10^{-31} W/H) for the diffuse component.

total column density of hydrogen, the background level should be the mid-infrared flux for zero column density of hydrogen. If we apply this to the data the uncertainty on the background will be large because the dynamical range of the ISOCAM images is small ($\lesssim 0.6$ MJy/sr). Further, in fields B and C, CO emission cannot be considered as a quantitative tracer of the H$_2$ column density. In this context, we chose to work in relative brightness for all tracers. This means that, for each field and for gas and dust maps, we subtract an offset taken in a common region where the mid-IR emission is the lowest.

5. Variation of the mid-infrared emissivity with gas velocity

In this section we show that the spatial shift between the dust and gas tracers in field A, and therefore the dispersion in the LW2-$N_{\rm H I}$ and LW3-$N_{\rm H I}$ relations, can be accounted for by a difference in the small dust particles emissivity per H atom between the two H I kinematic components (see § 3.1.2).

As seen in Fig. 7, the two H I components identified earlier with the Gaussian decomposition have very different column density profiles across field A. If we consider the morphology of both components, the mid-infrared emission is more similar to the filament than to the diffuse H I component. By giving different emissivity to these two H I components we were able to reproduce rather well the mid-infrared profiles (see Fig 11 and 12). The LW2 and LW3 emissivities that best reproduce the mid-infrared observations are detailed in Table 2.

The comparison of the mean emissivity of typical Galactic cirrus of the solar neighborhood obtained at 12 μm by Boulanger & Pérault (1988) with the LW2 and LW3 emissivities ($4\pi\nu e_\nu$ in W/H) deduced here, shows that the diffuse component of field A has an emissivity very similar to the average cirrus value. On the other hand, the filamentary component seems to have an emissivity 5 ± 1 (LW2) and 2.5 ± 0.5 (LW3) times higher than the average value. From the numbers of Table 2 we also conclude that the ratio of the LW2 and LW3 emissivity is ~ 0.9 in the diffuse gas and ~ 1.8 in the filament. Because of the good spatial correlation between the 100 μm and H I column density (see Fig. 5), the large grains responsible for the 100 μm emission must have the same emissivity in the the filamentary and diffuse components.

6. Abundance variations of small dust grains in an H I-**H$_2$** interface

Fields B and C cross an interface between a mainly atomic region and another one where significant CO emission is detected. The emission in field B is very uniform; it is thus difficult to correlate variations in the dust and gas emissions. Therefore, our whole analysis of the H I-H$_2$ transition will be based on the observations of field C.

To estimate the dust mid-infrared emissivity, we usually rely on an estimate of the gas column density. In field C, the structure of the gas is dominated by the molecular component. Because the determination of the CO to H$_2$ ratio is poorly constrained and because, in such diffuse clouds, it is known that CO is not such a good tracer of
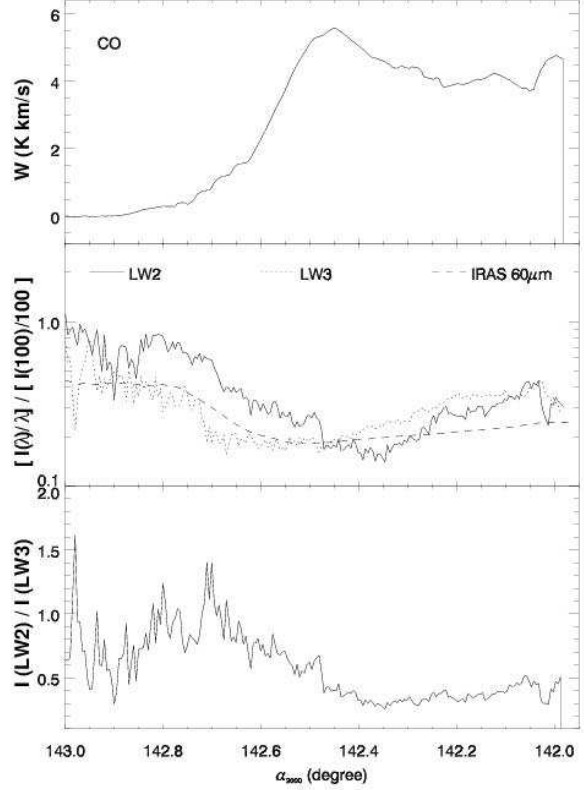
Field	λ (μm)	Component	$4\pi\nu e_\nu$ $(10^{-31}$ W/H)
A	6.5 (LW2)	average	3.8 ± 0.5
		filament	4.6 ± 0.3
		diffuse gas	0.9 ± 0.3
	15.0 (LW3)	average	2.3 ± 0.1
		filament	2.5 ± 0.3
		diffuse gas	1.0 ± 0.3
C	6.5 (LW2)	HI	1.9 ± 0.2
		CO	0.48 ± 0.05
	15.0 (LW3)	HI	1.3 ± 0.1
		CO	0.61 ± 0.06
high latitude	12.0		1.1 ± 0.3
	100.0		3.2 ± 0.1

Table 2. Emissivity in LW2 and LW3 in fields A and C. The 12 and 100 μm emissivity of typical high latitude Galactic cirrus (Boulanger & Pérault, 1988) are also given as a comparison. The uncertainties on the emissivity for the diffuse and filamentary components of field A reflect the uncertainties we have on the determination of the background emission. The uncertainty on the average emissivity of field A has been computed using the bootstrap method (Efron & Tibishirani, 1986) on the LW2-N_{HI} and LW3-N_{HI} relations of Fig. 10. The uncertainty on the emissivities of field C reflects the variations of the emissivity values over the region where they were measured.

Fig. 13. **Top:** Mean CO emission of the western part of field C, as a function of α_{2000}. **Middle:** Ratio $(I_{lw2}/6.5)/(I_{100}/100)$, $(I_{lw3}/15)/(I_{100}/100)$ and $(I_{60}/60)/(I_{100}/100)$ as a function of α_{2000}. **Bottom:** Ratio of the LW2 over LW3 emission as a function of α_{2000}.

the molecular column density (Reach et al., 1994), we prefer to compare the mid-infrared emission with the IRAS 100 μm band emission to estimate the abundance of the smallest dust particles, relative to that of bigger grains responsible for the emission at 100 μm.

In Fig. 13 (middle panel) we show the ratio $(\nu I_\nu)_\lambda/(\nu I_\nu)_{(100\mu m)}$ for LW2 (λ=6.5 μm), LW3 (λ=15 μm) and IRAS 60 μm, across the HI-H$_2$ transition. This way of presenting the data emphasizes the variation of dust emissivity at wavelength λ compared to the emissivity at 100 μm. If the grain properties and the heating are homogeneous, this ratio reflects changes in the relative abundance of grains. For all three wavelengths a decrease in the $(\nu I_\nu)_\lambda/(\nu I_\nu)_{(100\mu m)}$ ratio is observed, correlated with the increase of the CO emission. Furthermore, for the three bands, the lowest $(\nu I_\nu)_\lambda/(\nu I_\nu)_{(100\mu m)}$ is observed near the CO peak emission.

By making the assumption that the 100 μm emissivity is that measured by Boulanger & Pérault (1988) for the high latitude clouds (see Table 2), which is in accordance with the 100 μm emissivity estimated in that cloud by Joncas et al. (1992), we were able to estimate the emissivity in the LW2 and LW3 bands from the $(\nu I_\nu)_\lambda/(\nu I_\nu)_{(100\mu m)}$ ratio. In Table 2 we list an estimate of the mean LW2 and LW3 emissivity values for the atomic and molecular regions of the HI-H$_2$ transition. We estimate that the ratio of the emissivity in the HI region compared to the CO region is 4.0 ± 0.8 and 2.1 ± 0.4 in LW2 and LW3 respectively.

The ratio of the LW2 over LW3 emission for field C is also shown in Fig 13. In the purely atomic part of the fields, the ratio is ~ 0.8 and it drops to ~ 0.3, in a few 0.1pc, as we enter the molecular region.

7. Discussion

The comparison of the mid-infrared, HI, CO and IRAS observations has allowed us to highlight important spatial variations of the small dust particles emissivity in the Ursa Major cirrus.

7.1. Spatial variation of the mid-infrared emissivity

The Ursa Major cirrus is characterized by a low gas column density (6.0×10^{20} cm^{-2}- corresponding to $A_V \approx 0.3$) and the absence of star formation. In this context, the spatial variations in the mid-infrared emissivity can result from either (1) the presence of molecular gas or very cold HI gas or (2) an attenuation of the UV radiation field on scales smaller than the beam size or (3) variations in the small grains abundance or emission properties. The good correlation observed between the HI and

$100\mu m$ emissions in Fig. 5 puts constraints on hypothesis (1) and (2). Dust associated with molecular gas should produce an excess of IR emission with respect to the IR-HI correlation. However, this excess could be reduced by an attenuation of the UV radiation field in the same regions since molecules are expected to be present in the most shielded parts of the cloud. But both effects would modify the mid-infrared and $100\ \mu m$ emission in the same way. Therefore, variations of the dust size distribution or of emission properties (hypothesis (3)) are more directly traced by the mid-infrared to $100\ \mu m$ emission ratio than the mid-infrared emissivity per H atom. However it is only with the HI emission that we have access to the velocity information.

In field A, the emissivities in the LW2 and LW3 filters are enhanced by a factor 5 ± 1 and 2.5 ± 0.5 in the filament with respect to the more diffuse atomic gas. Since such a change is ruled out for large grain emission at $100\ \mu m$, we interpret the LW2 and LW3 emissivity variations as an evidence for variations in the small grains characteristics (abundance/emission properties). Elements are still lacking to identify whether the emissivity variations oberved here are due to variations in the abundance of the mid-infrared emitters or to their emission properties. We recall that this filament has a very peculiar kinematic: a large velocity gradient across the filament which could be a signature of a fast rotation around its long axis. We discuss below how large velocity gradients might enhance the abundance of small dust grains.

Based on the mid-infrared to $100\ \mu m$ ratio, in field C, the abundance of the particles emitting in the LW2 and LW3 filters are found to be respectively 4.0 ± 0.8 and 2.1 ± 0.4 times lower in the molecular region than in the atomic gas. A similar effect is also observed with the IRAS $60\ \mu m$ emission.

7.2. Turbulence and dust size distribution

We discuss here a possible link between the dust size distribution and the kinematics of the gas (i.e. the importance of the turbulent motions). The filament in field A, which has an aspect ratio of the order of 10 (Miville-Deschênes, 1999), is reminiscent of coherent structures of vorticity observed in turbulence and thought to be responsible for the phenomenon of intermittency (Vincent & Meneguzzi, 1994). Falgarone & Puget (1995) investigated the decoupling of dust and gas in a turbulent flow as a function of grain size. They showed that the intermittency of turbulence enhances the decoupling of small dust grains from the gas motions because of the non-Gaussian distribution of the velocity gradients. Thus the relative velocities of small dust particles can be significantly increased above that reached in a Kolmogorov turbulence. Qualitatively, the collision outcome is coagulation or grain fragmentation below and above some energy threshold. In these regions, the relative velocities might become sufficiently large that small dust grains are produced by grain fragmentation in

grain-grain collisions. The high abundance of small dust particles in the filament of field A could be a signature of such a fragmentation process. In the molecular gas, where the turbulent motions are smaller than in the HI gas (Fig. 9), we may observe the reverse process: mutual coagulation of small grains could occur which would explain the drop of the mid-infrared emissivity.

The outcome of a grain-grain collision (coagulation, bouncing or fragmentation) depends on the kinetic energy of the colliding grains, on their respective masses and on their material. Based on a numerical simulation of aggregate growth, Dominik & Tielens (1997) have showed that two $\sim 0.1\ \mu m$ aggregates stick if their relative velocity is $\delta v \lesssim 0.8$ km s^{-1}. But if it is higher than ~ 1 km s^{-1}, the dust aggregates start to fragment.

Following Draine (1985), the typical relative velocity of two grains of size a_1 in a Kolmogorov turbulent flow characterized by a velocity dispersion v_{max} at a scale l_{max} is given by the following equation:

$$v_{rel} = \left(\frac{v_{max}^{3/2}}{l_{max}^{1/2}}\right)\left(\frac{a_1\rho_{gr}}{4n}\right)^{1/2}\left(\frac{2\pi}{\mu kT}\right)^{1/4}, \qquad (2)$$

where n and T are the gas density and temperature and ρ_{gr} is the grain mass density. If we consider standard values for an HI cloud like Ursa Major ($n = 100$ cm^{-3}, $T = 200$ K) and Kolmogorov turbulence with $l_{max} = 10$ pc and $v_{max} = 5$ km s^{-1}, the typical relative velocity for big grains ($a_1 = 0.1\ \mu m$ and $\rho_{gr} = 3$ g cm^{-3}) would be $v_{rel} \approx 0.6$ km s^{-1}, which is close to the fragmentation threshold established by Dominik & Tielens (1997). But in field A, we observe velocity gradients of 5 and 10 km s^{-1} pc^{-1}, which are larger than the gradients characteristic of Kolmogorov turbulence at the scale of the filament (0.3 pc). As shown by Falgarone & Puget (1995), these local large velocity gradients may increase the relative velocity between small grains. Considering the strength of the velocity gradient observed here, it is very likely that the relative velocity between large grains exceeds the fragmentation threshold.

In field C, the width of the CO line is ~ 1.5 km s^{-1} (see Fig. 9). If we consider that this width is mostly due to turbulence and that the thickness of the Ursa Major cirrus is ~ 2 pc, the typical velocity dispersion of $0.1\ \mu m$ grains for the same temperature and density as in field A is ~ 0.2 km s^{-1} . This is lower than the coagulation threshold determined by Dominik & Tielens (1997) and it could be even lower since the density in the molecular region is higher than the mean cirrus value.

This indicates that fragmentation and coagulation by grain-grain collisions in a turbulent flow may be at the origin of the abundance variations of small dust grains observed in the Ursa Major cirrus. To estimate the timescales over which the dust size distribution is significantly affected by this process, one should take into account the collisions between grains of all sizes and, in the case of fragmentation, make some hypothesis on the size distribution of the fragments. This is beyond the scope of the

present paper. Draine (1985) has estimated the depletion time scale of small grains in interstellar clouds to be $\sim 10^6$ years by considering only sticking on large grains in Kolmogorov turbulence. Mutual coagulation of small grains actually occurs faster if we take intermittency into account (Falgarone & Puget, 1995).

7.3. Variations of the $I_\nu(\mathrm{LW2})/I_\nu(\mathrm{LW3})$ ratio

In addition to the spatial variations of the mid-infrared emissivity we have also observed spatial variations of the $I_\nu(\mathrm{LW2})/I_\nu(\mathrm{LW3})$ ratio. For example, it is twice larger in the HI filament of field A than in the diffuse gas that surrounds it. It is also observed to be twice larger in the atomic side of the HI-H_2 transition than in the molecular region. Similar variations of the $I_\nu(\mathrm{LW2})/I_\nu(\mathrm{LW3})$ ratio are observed across photo-dissociation regions from the photo-dissociated gas to the molecular gas (Abergel et al., 2000).

Using broad-band filters and CVF observations of L1630, Abergel et al. (2000) showed that the emission in the LW2 filter is correlated to the intensity of the 7.7 μm aromatic band, and that the emission in the LW3 filter is correlated to the continuum level at 15 μm. These CVF data show that variations in the relative amplitude of the aromatic bands are minor and do not significantly affect the $I_\nu(\mathrm{LW2})/I_\nu(\mathrm{LW3})$. It is unclear whether the aromatic bands and continuum at 15 μm come from the same dust particles. Within the present understanding of the nature and emission properties of small dust grains it is impossible to determine the origin of the $I_\nu(\mathrm{LW2})/I_\nu(\mathrm{LW3})$ ratio variations.

7.4. Coagulation of small grains

Another example of the decrease of the small dust grain abundance in an HI-H_2 interface is given by Bernard et al. (1999) who characterize dust properties, in a section of the Polaris cirrus with moderate opacity ($A_V \sim 1$), by combining IRAS and far-IR/sub-mm observations. In this cloud, there is no mid-IR emission, the 60/100 μm emission ratio is low and the large grain temperature, 13 K, is lower than the mean cirrus value 17.5 K. These dust properties are characteristic of dense gas within molecular clouds. Bernard et al. (1999) explain these observations by the formation of large fractal grains through the coagulation of small dust grains on large grains. The decrease of the small dust grains abundance in the HI-H_2 interface of the Ursa Major cirrus could be an intermediate step in the dust evolution, between the diffuse HI and denser environments.

8. Conclusion

We have presented ISOCAM images (in two filters LW2 (5-8.5 μm) and LW3 (12-18 μm)) of a high Galactic latitude cirrus transparent to stellar photons. The angular

resolution and brightness sensitivity of these images improve by one order of magnitude those provided by the 12 and 25 μm IRAS images. We have compared the ISOCAM images with HI, CO and 100μm observations to measure the mid-IR emissivity (mid-IR emission from small dust particles per hydrogen atom) for distinct gas velocity components and across an interface between atomic and molecular gas. We find significant variations in the mid-IR emissivity which we interpret as changes in the abundance of small grains within the cloud. The abundance of the small dust particles is larger by a factor 5 within a filament with a strong transverse velocity gradient, than in the surrounding diffuse HI. We propose that this abundance enhancement results from the formation of small dust grains through the fragmentation of larger grains in energetic grain-grain collisions induced by turbulence. The abundance of small dust particles with respect to the larger grains is observed to be reduced (by a factor 4) in CO emitting molecular gas with respect to its value in diffuse HI. In this gas the turbulent motions have a smaller amplitude than in the HI gas. Within the proposed interpretation, we speculate that in such an environment grain/grain collisions are less energetic and they therefore lead to coagulation and not fragmentation.

Spectroscopic observations indicate that the LW2/LW3 color ratio measures the contrast of the aromatic bands with respect to the underlying continuum emission. A drop in the $I_\nu(\mathrm{LW2})/I_\nu(\mathrm{LW3})$ ratio by a factor ~ 2 is observed from the HI filament to the diffuse HI gas and from the HI to the H_2 gas across the HI-H_2 interface. The LW2/LW3 color ratio is observed to decrease with the mid-IR emissivity. If the band contrast decreases for increasing particles sizes, a plausible assumption in terms of solid state physics, the mid-IR emissivity and color variations could both be related to a change in the small-sizes end of the dust size distribution.

References

Abergel, A., Bernard, J. P., Boulanger, F., Miville-Deschênes, M. A., Puget, J. L., Nordh, L., Olofsson, G., Huldtgren, M., Kaas, A. A., Falgarone, E., Pérault, M., André, P., Montmerle, T., Copet, E., Persi, P. & Sibille, F. The extended infrared emission of the

southern parts of orion b. In R. J. Laureijs, K. L. & Kessler, M. F, editors, *ISO Beyond Point Sources: Studies of Extended Infrared Emission*, page 119, ISO Data Centre, Villafranca del Castillo, Madrid, Spain, 2000.

Bakes, E. L. O. & Tielens, A. G. G. M. 1994, ApJ, 427, 822.

Bernard, J. P., Abergel, A., Ristorcelli, I., Pajot, F., Torre, J. P., Boulanger, F., Giard, M., Lagache, G., Serra, G., Lamarre, J. M., Puget, J. L., Lepeintre, F. & Cambrésy, L. 1999, A&A, 347, 640.

Boulanger, F. & Pérault, M. 1988, ApJ, 330, 964.

Boulanger, F., Falgarone, E., Puget, J. L. & Helou, G. 1990, ApJ, 364, 136.

de Vries, H. W., Thaddeus, P. & Heithausen, A. 1987, ApJ, 319, 723.

Dominik, C. & Tielens, A. G. G. M. 1997, ApJ, 480, 647.

Draine, B. T. Grain evolution in dark clouds. In *Protostars and planets II*, page 621, Tucson, AZ, 1985. University of Arizona Press.

Duley, W. W. & Williams, D. A. 1993, MNRAS, 260, 37.

Duley, W. W. 1996, MNRAS, 279, 591.

Efron, B. & Tibishirani, R. 1986, Stat. Sci., 1, 54.

Falgarone, E. & Puget, J. L. 1995, A&A, 293, 840.

Heiles, C. 1989, ApJ, 336, 808.

Henning, T. In L. d'Hendecourt, C. J. & Jones, A, editors, *Solid Interstellar Matter: The ISO Revolution*, page 247, Les Houches, 1999. EDP Sciences and Springer-Verlag.

Joncas, G., Boulanger, F. & Dewdney, P. E. 1992, ApJ, 397, 165.

Miville-Deschênes, M. A., Boulanger, F., Abergel, A. & Bernard, J. P. 2000, A&As, 146, 519.

Miville-Deschênes, M. A., Joncas, G., Boulanger, F. & Falgarone, E. in preparation, 2001.

Miville-Deschênes, M. A. PhD thesis, Université Paris XI (France) and Université Laval (Québec), 1999.

Pound, M. W. & Goodman, A. A. 1997, ApJ, 482, 334.

Reach, W. T., Koo, B. C. & Heiles, C. 1994, ApJ, 429, 672.

Spitzer, L. 1978, *Physical processes in the interstellar medium*. Wiley-Interscience, New York.

Vincent, A. & Meneguzzi, M. 1994, J. Fluid Mech., 258, 245.